AMERICAN SOCIETY FOR MICROBIOLOGY | mSystems®

RESEARCH ARTICLE
Novel Systems Biology Techniques

Simultaneous Tracking of *Pseudomonas aeruginosa* Motility in Liquid and at the Solid-Liquid Interface Reveals Differential Roles for the Flagellar Stators

Andrew L. Hook,[a] James L. Flewellen,[b,c,d] Jean-Frédéric Dubern,[e] Alessandro M. Carabelli,[a,e] Irwin M. Zaid,[d] Richard M. Berry,[d] Ricky D. Wildman,[f] Noah Russell,[g] Paul Williams,[e] Morgan R. Alexander[a]

[a]Advanced Materials and Healthcare Technologies Division, School of Pharmacy, University of Nottingham, Nottingham, United Kingdom
[b]Immune Receptor Activation Laboratory, The Francis Crick Institute, London, United Kingdom
[c]Division of Immunology and Inflammation, Department of Medicine, Imperial College London, London, United Kingdom
[d]Department of Physics, Clarendon Laboratory, University of Oxford, Oxford, United Kingdom
[e]Centre for Biomolecular Sciences, School of Life Sciences, University of Nottingham, Nottingham, United Kingdom
[f]Department of Chemical and Environmental Engineering, School of Engineering, University of Nottingham, Nottingham, United Kingdom
[g]Marine Biological Association, The Laboratory, Plymouth, United Kingdom

ABSTRACT Bacteria sense chemicals, surfaces, and other cells and move toward some and away from others. Studying how single bacterial cells in a population move requires sophisticated tracking and imaging techniques. We have established quantitative methodology for label-free imaging and tracking of individual bacterial cells simultaneously within the bulk liquid and at solid-liquid interfaces by utilizing the imaging modes of digital holographic microscopy (DHM) in three dimensions (3D), differential interference contrast (DIC), and total internal reflectance microscopy (TIRM) in two dimensions (2D) combined with analysis protocols employing bespoke software. To exemplify and validate this methodology, we investigated the swimming behavior of a *Pseudomonas aeruginosa* wild-type strain and isogenic flagellar stator mutants (*motAB* and *motCD*) within the bulk liquid and at the surface at the single-cell and population levels. Multiple motile behaviors were observed that could be differentiated by speed and directionality. Both stator mutants swam slower and were unable to adjust to the near-surface environment as effectively as the wild type, highlighting differential roles for the stators in adapting to near-surface environments. A significant reduction in run speed was observed for the *P. aeruginosa mot* mutants, which decreased further on entering the near-surface environment. These results are consistent with the *mot* stators playing key roles in responding to the near-surface environment.

IMPORTANCE We have established a methodology to enable the movement of individual bacterial cells to be followed within a 3D space without requiring any labeling. Such an approach is important to observe and understand how bacteria interact with surfaces and form biofilm. We investigated the swimming behavior of *Pseudomonas aeruginosa*, which has two flagellar stators that drive its swimming motion. Mutants that had only either one of the two stators swam slower and were unable to adjust to the near-surface environment as effectively as the wild type. These results are consistent with the *mot* stators playing key roles in responding to the near-surface environment and could be used by bacteria to sense via their flagella when they are near a surface.

KEYWORDS 3D imaging, biofilms, digitial holographic microscopy, flagellar motility, stators

Citation Hook AL, Flewellen JL, Dubern J-F, Carabelli AM, Zaid IM, Berry RM, Wildman RD, Russell N, Williams P, Alexander MR. 2019. Simultaneous tracking of *Pseudomonas aeruginosa* motility in liquid and at the solid-liquid interface reveals differential roles for the flagellar stators. mSystems 4:e00390-19. https://doi.org/10.1128/mSystems.00390-19.

Editor Seth Bordenstein, Vanderbilt University

Address correspondence to Paul Williams, paul.williams@nottingham.ac.uk, or Morgan R. Alexander, morgan.alexander@nottingham.ac.uk.

Received 28 June 2019
Accepted 1 September 2019
Published 24 September 2019

Flagellum- and type IV pilus (TFP)-mediated motility enables bacteria to migrate toward nutrients or away from toxic substances (1, 2) and plays key roles in bacterial biofilm formation and host-pathogen interactions (3, 4). In addition, these bacterial appendages also play a role in surface sensing (5). The mechanisms by which individual cell behaviors drive social phenomena such as swarming, twitching, and biofilm development have been the subject of intense investigations (3–15). The ability to collect data simultaneously on individual bacterial cells in a population that includes both planktonic and surface-attached cells will facilitate the acquisition of spatiotemporal dynamics that will aid our understanding of the signal transduction mechanisms that drive bacterial social behaviors.

Pseudomonas aeruginosa is a Gram-negative rod-shaped cell with a single polar flagellum that employs a number of different mechanisms for moving through liquids and across surfaces. These include flagellum-mediated swimming, spinning, near-surface swimming and swarming, TFP-mediated twitching (crawling and walking), gliding (active movement without the use of flagella or pili), and sliding, i.e., passive movements over surfaces through the use of surfactants (8, 16). Flagella are also associated with bacterial surface mechanosensing and play a key role during the early stages of biofilm formation (11, 12, 14, 15, 17). In *P. aeruginosa*, the flagellum, in contrast to the case with most other bacterial species, is driven by two (rather than one) stator complexes termed MotAB and MotCD. These are the static elements of the bacterial motor that generate torque for flagellar rotation powered by proton motive force (18). Either MotAB or MotCD is sufficient for swimming, but the two stators make differential contributions to swarming motility and biofilm formation (15, 19, 20). Deletion of *motCD*, but not *motAB*, renders *P. aeruginosa* incapable of swarming over agar at concentrations above 0.5% (20), suggesting that the MotCD stator complex is able to apply torque more efficiently than the MotAB complex (11, 19, 20). Both stators are required for biofilm formation (15).

Recent studies suggest an interaction between MotCD and the second messenger cyclic diguanylate (c-di-GMP), which plays a key role in driving the lifestyle switch of motile *P. aeruginosa* cells toward surface-associated biofilm formation (21), through the PilZ domain-containing protein FlgZ (6). This interaction may cause the MotCD stator to be displaced from the flagellar motor or may increase the likelihood of this event occurring (11). Moreover, free MotC is able to interact with the c-di-GMP receptor, SadC, causing it to become activated, triggering further production of c-di-GMP (17). This produces a positive-feedback loop mediated by the flagellar machinery that directs cells from the motile to the sessile state, with stator exchange playing a key signaling role. MotAB is also necessary for triggering type IV pilus formation after cell attachment, further implying a role for both stators in surface sensing (4). The contribution of flagellar stators as surface sensors for biofilm formation, which involves increasing production of c-di-GMP and pili, has also been observed for the single stator species *Caulobacter crescentus* (9, 22). Understanding the respective roles of MotAB and MotCD in the initial interactions of swimming cells with surfaces is important particularly in the context of early-stage biofilm formation.

Cell tracking in three dimensions (3D) allows for a complete analysis of bacterial movement and can be used to assess the trajectory of a bacterium approaching or leaving a surface. Early work following single cells determined the z-position by tracking the focal plane of a bacterium and recording x and y movements optically. This method can follow only a single cell at a time and is thus unable to record the movement of many cells in a population (23). 3D volumes have been imaged using optical techniques with narrow focal planes such as confocal microscopy to acquire z-stacks, but this approach is limited by low light transmission and consequently low acquisition rates. Alternatively, "lookup" tables have been used to match the image of an object with reference images taken at known distances away from the focal plane of an object (24–26).

Most recently, 3D tracking of bacteria has been achieved using digital holographic microscopy (DHM) in which the x-, y-, and z-positions of individual cells are captured via

recorded diffraction patterns and determined computationally (27, 28). For the monotrichous *P. aeruginosa*, swimming in liquids has been analyzed using DHM where motility patterns have been classified as oscillation, meander, helix, pseudohelix, and twisting (27). The key advantage of DHM is its ability to observe the 3D trajectories of many cells in a bacterial population simultaneously; however, features such as their orientation and shape are difficult to ascertain from the holograms. A recent variant using a three-laser setup permitted the use of DHM for determining bacterial volume and orientation throughout a 3D space. However, this approach has thus far been demonstrated only for the analysis of single bacterial cells released near a surface using optical tweezers (29).

To gain novel insights into the differences in cell behavior within the bulk and at the surface, it is necessary to image both environments concurrently. To achieve this, we developed a novel multimode 2/3D microscope with interlaced acquisition of 2D surface differential interference contrast (DIC) or total internal reflectance microscopy (TIRM) images with 3D DHM. The spatial and temporal resolutions of the DIC images at the surface were sufficient to allow the bacterial cell orientation to be determined, while TIRM imaging confirmed the close proximity to the surface (<200 nm) of near-surface swimming cells. In addition, to enable imaging of a higher-density bacterial population than is possible for DHM, we incorporated an optical relay (30) to recreate the sampling area virtually, enabling it to be rapidly scanned in the z-dimension using a remote piezo-driven objective to avoid sample disturbance. A schematic of the multimode 2/3D microscope setup is shown in Fig. 1A and B. Using this methodology we were able to simultaneously determine the individual cell orientation and proximity to the surface as well as the 3D location of cells at low and high densities over time. To exemplify the utility of this system, the microscope was used to explore the respective contributions of the *P. aeruginosa* MotAB and MotCD stators to bulk liquid movement and interactions at the solid-liquid interface.

RESULTS

Imaging of individual *P. aeruginosa* cells in the bulk liquid and at the solid-liquid interface. To characterize *P. aeruginosa* motility using the multimode microscope, interlaced capture of either 2D DIC or TIRM at the surface and 3D in-line DHM images in the bulk liquid, respectively, was conducted within 5 min of motile cells being added to the sample chamber (Fig. 1C) at 41.7 Hz (total frame rate). At this rate, bacterial fluctuating motion was undersampled (body and Brownian motion) but directional motion was oversampled (see Fig. S1 in the supplemental material). After data acquisition, bacterial trajectory generation was achieved using bespoke Matlab scripts (DHMTracking and StackMaster). Using this approach, trajectories could be captured within the bulk medium (Fig. 2A) and at the glass surface-liquid interface (Fig. 2C and D). Figure 2B illustrates the DIC z-stack of bacterial cell 3D positions at inoculation and after 4 h of growth using the remote image relay to demonstrate that single cells in dense populations can be located. Using DIC imaging at the surface, the orientation of the bacterial cells could also be determined to establish whether a cell was orientated in the direction of travel and if cells were attached via their long axes or poles (Fig. 2C). TIRM allowed the observation of cells within a close proximity to the surface since objects were detected only within the depth of penetration of the evanescent wave into the bulk liquid (200 nm in the configuration used [Fig. 3A]). The trajectories of the cells in a bacterial population were observed through the interlaced capture of DHM and DIC images. The resulting tracks were combined and, where bacteria approached the surface, information from both the DHM and DIC images was included. An example of a track travelling from the bulk to the surface is shown in Fig. 2D.

Single-cell bacterial trajectories were determined using DHM (Fig. 2A) at cell densities of up to 1.7×10^4 cells/μl, but above this, overlapping interference patterns prevented digital holographic reconstruction. To measure the 3D distribution of cells at higher populations we used the remote image relay to acquire a series of DIC images

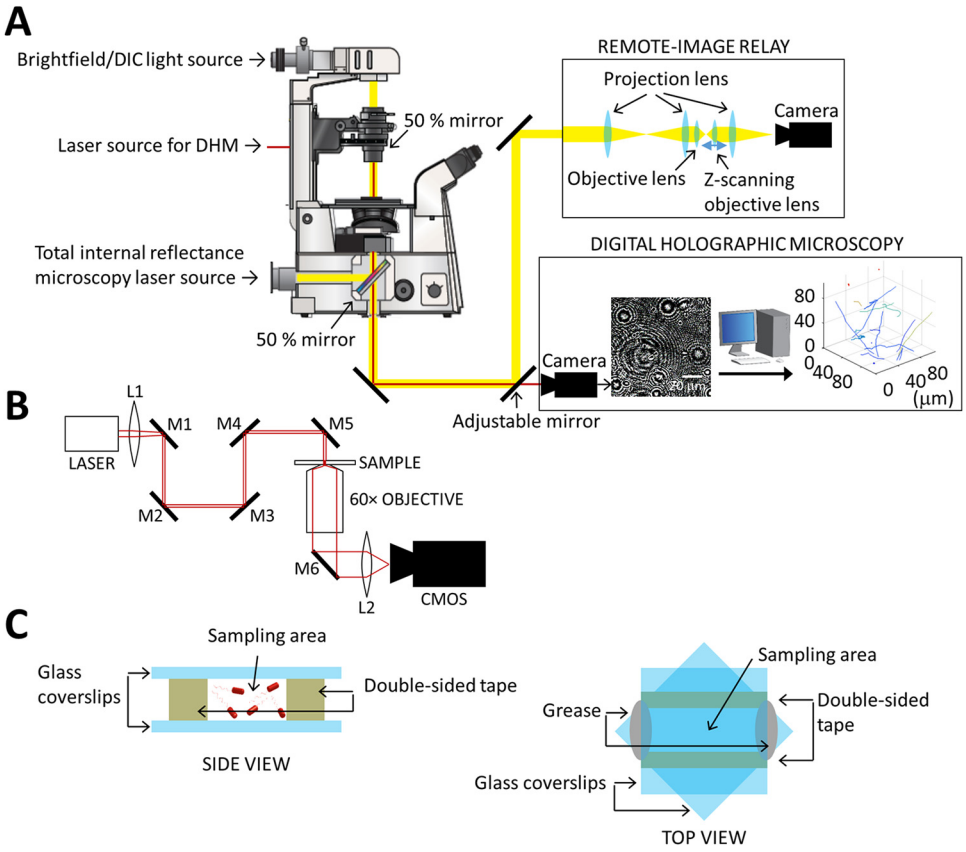

FIG 1 Overview of the experimental setup. (A) Schematic of the multimode 2/3D microscope used in this study, including the optical ensemble for the remote-image relay. The remote-image relay allows scanning of the focal plane to reconstruct z-stacks without disturbing the sample. The microscope is also equipped with lasers to enable digital holographic microscopy (DHM) and total internal reflectance microscopy (TIRM). (B) A schematic diagram of the light path used for in-line DHM. The positions of L1, M1, and M2 were adjustable to alter the position and focus of the laser. (C) Schematic of the sample format used in this study, including side and top views. The z-height of the sample volume (distance between glass slides) was 100 μm. The typical separation between the two strips of double-sided tape was 5 mm. The two coverslips were orientated at 45° to each other to enable the easy sealing of the channel ends with hydrocarbon grease.

separated in the z-axis, referred to as z-stacks. Analysis of the z-stack data enabled the position of each bacterium to be determined at a population density of 3.7×10^5 cells/μl, greater than an order of magnitude improvement over DHM, with a maximum population density within any one image of 8.0×10^5 cells/μl. This enabled the growth of a *P. aeruginosa* cell culture to be followed over 4 h (Fig. 2B). Objects that were vertically contiguous for adjacent frames were attributed to a single bacterium and the position of each bacterial cell was determined as the center of mass calculated from all pixels taken for combined objects. We employed a z-spacing of 1 μm in order to ensure that we did not omit bacterial cells when imaging (typical cell dimensions = 2 by 5 μm; depth of field at a magnification of ×60 with a numerical aperture [NA] of $1.4 \approx 0.6$ μm). Over a z-range of 100 μm and a maximum imaging rate of 100 Hz, this meant that the maximum acquisition rate using the DIC z-stack was 1 Hz. Although useful for determining cell population density and distribution, the lower acquisition rate of this approach compared to that of DHM made it impractical for tracking fast-swimming bacteria since, for accurate tracking, bacteria should not travel further than their dimensions per frame, thus limiting this approach to cell movement slower than 5 μm/s. Consequently, DIC z-stacks were not used for tracking in this study but rather to assess cell distribution at high cell density.

Characterization of bacterial trajectories. A number of different bacterial swimming trajectories were readily visually discernible within *P. aeruginosa* populations

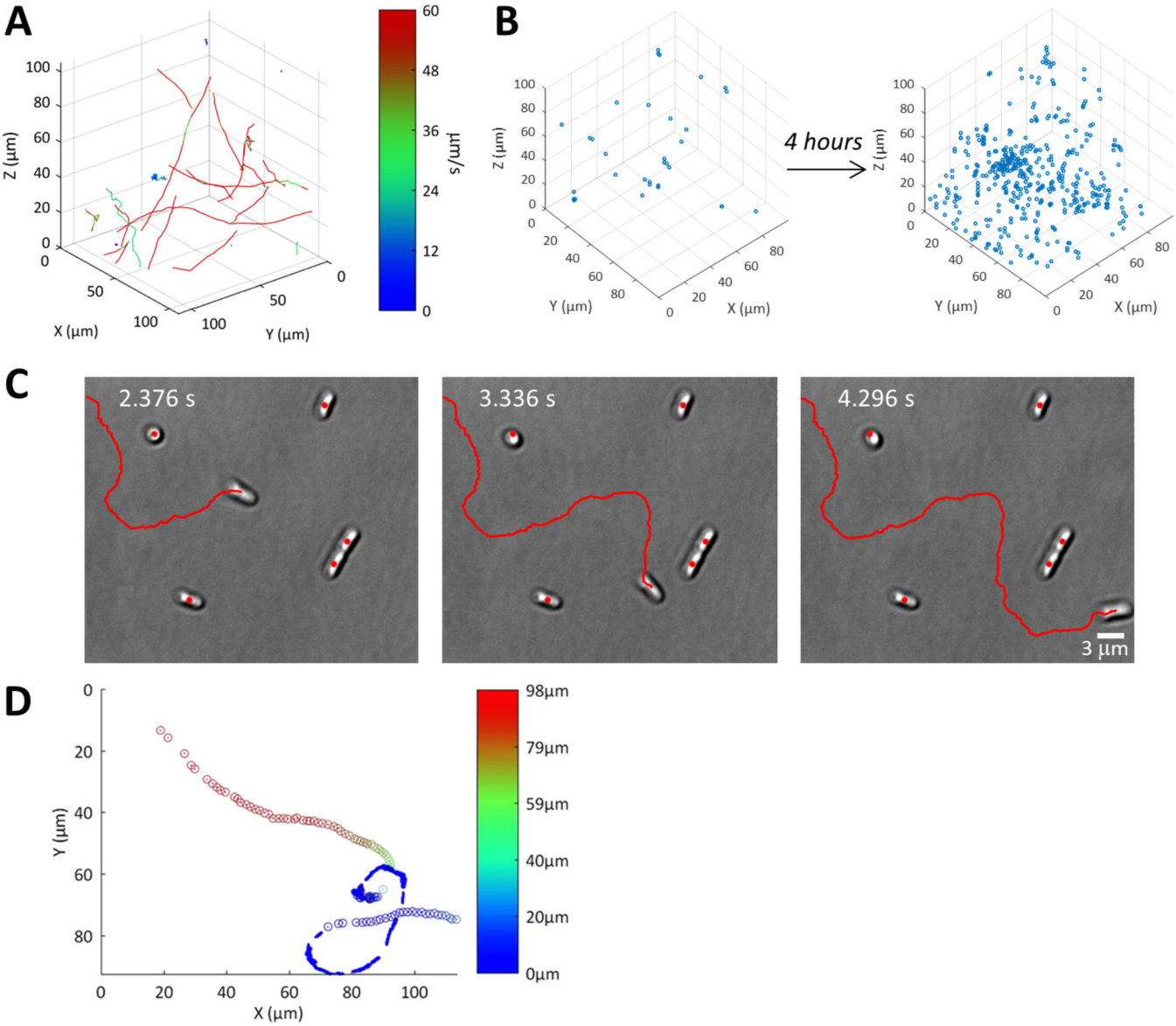

FIG 2 2D and 3D imaging of *P. aeruginosa* wild-type bacterial trajectories. (A) DHM isometric view of bacterial trajectories for one continuous 20-s acquisition at 41.7 Hz. Trajectories have been colored by the instantaneous speed of the track according to the intensity scale provided. (B) DIC z-stack of instantaneous bacterial 3D positions at seeding conditions and after 4 h of incubation acquired using the remote-image relay, illustrating the high cell density that can be located and tracked using this method. (C) DIC image sequence of *P. aeruginosa* cells swimming at the glass surface, with 960 ms between images shown (complete image sequence is available in Movie S1 in the supplemental material). The trajectory is shown in red. Of note is the change in bacterial orientation, which matched the change in direction during the journey. The image sequence also contains examples of long-axis (side)- and polar (end)-attached cells. The center of mass of each cell at 2.376 s is indicated as a red dot in each frame; the center of mass of side-attached cells remained unchanged, whereas a change in center of mass location was observed for the end-attached cell. (D) Example of a bacterial trajectory where a cell approached the surface from the bulk. The z-position of the bacteria is colored according to the intensity scale. The center of mass as determined by DHM measurements is shown as a circle. When the bacteria came close enough to the surface, the dimension of the bacteria was plotted as determined by DIC. All bacterial positions have been overlaid.

(Fig. 2A and Fig. 4). Relatively straight trajectories with cells travelling at high speeds are referred to as runs after the convention of Berg et al. (2, 31) (Fig. 4A). Cells swimming parallel to the surface were termed near-surface runs (Fig. 4B), a phenomenon that has been assigned to various mechanisms, including hydrodynamic interactions, Brownian motion, and surface contact (25, 32, 33). Visual inspection of the tracks indicated that near-surface runs had a greater incidence of directional-change events than those observed in the bulk, where trajectories were straighter for longer. Moreover, we observed circular trajectories where bacteria were travelling at the surface, consistent with previous observations (Fig. 4B); curved near-surface runs have previously been attributed to flagellum-mediated surface interactions (7).

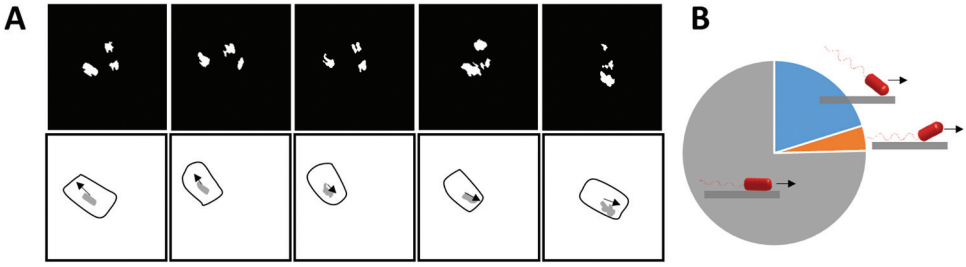

FIG 3 Interlaced capture of near-surface swimming bacteria with TIRM and DHM. (A) TIRM image sequence showing a direction reversal. There was a time interval of 40 ms between each displayed frame. The complete image sequence is available in the supplemental material (Movie S2). Images shown have been binarized, and objects with an area less than 100 pixels, deemed to be noise, were removed. To aid in visualization, the outline (determined from DHM) of the moving cell is shown beneath the corresponding composite image along with the smoothed area of the cell imaged by TIRM (gray). The displacement vector of the center of mass of the cell (determined from DHM) is also shown as an arrow. (B) Distribution of the position of the center of mass of the TIRM spot within the cell body for 9 cells observed to be swimming parallel to the surface over a total of 183 frames, either at the front pole (blue), in the middle (gray), or at the rear pole (orange) of the cell (shown schematically, where the arrows indicate the direction of travel of the bacterium). The front and rear of the cell were determined from the direction the bacterial cell was travelling subsequent to an image being taken. The TIRM spot was assigned as middle if it was less than 1 μm from the center of mass of the cell as determined by DHM.

Using TIRM, we showed that the bodies of near-surface-migrating bacteria were swimming parallel to the surface at a distance of less than 200 nm (Fig. 3A), a separation substantially shorter than the typical length of a flagellum ($\approx$5 μm [Fig. S2A]) (34). Through interlaced capture of DHM and TIRM imaging, the center of mass of the bacteria (as determined by DHM) and the center of mass of the contact point (as determined by TIRM) were compared (Fig. 3A). The majority of cells (75%) exhibited similar centers of mass and contact point, consistent with cells swimming parallel to the surface. In some cases, bacteria swam with either the front pole (20%) or the rear pole (4%) of the cell closer to the surface, defined by its direction of travel, consistent with the cell swimming front pole up or down (Fig. 3B). The measurements presented assume that the bacteria were in contact with the surface. This assumption was likely not true in all cases, such that the number of cells swimming front pole up or down may be underestimated. This observation of monotrichously flagellated *P. aeruginosa* differs from observations of the swimming of the peritrichously flagellated *Escherichia coli*, where all cells were reported to swim with the front pole down to the surface as estimated using 3-color DHM (29).

Away from the solid-liquid interface, an alternative class of swimming trajectory was observed, where the movement of the bacteria was slower than the near-surface runs and was characterized by frequent reversals of swimming direction, a phenomenon assumed to be caused by reversals of flagellar rotation (Fig. 4C), termed oscillating after the classification applied by Vater et al. (27). These oscillating bacterial cells were travelling at a reduced speeds of 12 ± 5 μm/s, substantially slower than the cells exhibiting run trajectories at 59 ± 4 μm/s. Notably, we did not observe oscillating cells at the surface, likely because the constraints of the proximal surface restricted the directional change of the cells upon flagellar reversal. Near-surface runs, which we term rambling, were slower and exhibited more frequent changes in direction than bulk runs. This rambling motion has not previously been reported. Rambling at the surface did not include the high frequency of directional reversals seen in the bulk (>90°) for oscillating cells.

Some cases were observed in which *P. aeruginosa* trajectories were reminiscent of peritrichously flagellated *Escherichia coli* run-and-tumble patterns (2, 31), whereby a straight "run" path was interspersed by a high frequency (2 Hz) of reversal events before the bacteria recommenced a run trajectory (Fig. S2B). The average reversal rate observed in the bulk population was 0.5 Hz. We observed no changes in the orientation of the bacterial body for surface reversal events (where the change in direction exceeded 120° [Fig. 4D]) observed at the glass surface (Fig. 4E), consistent with these

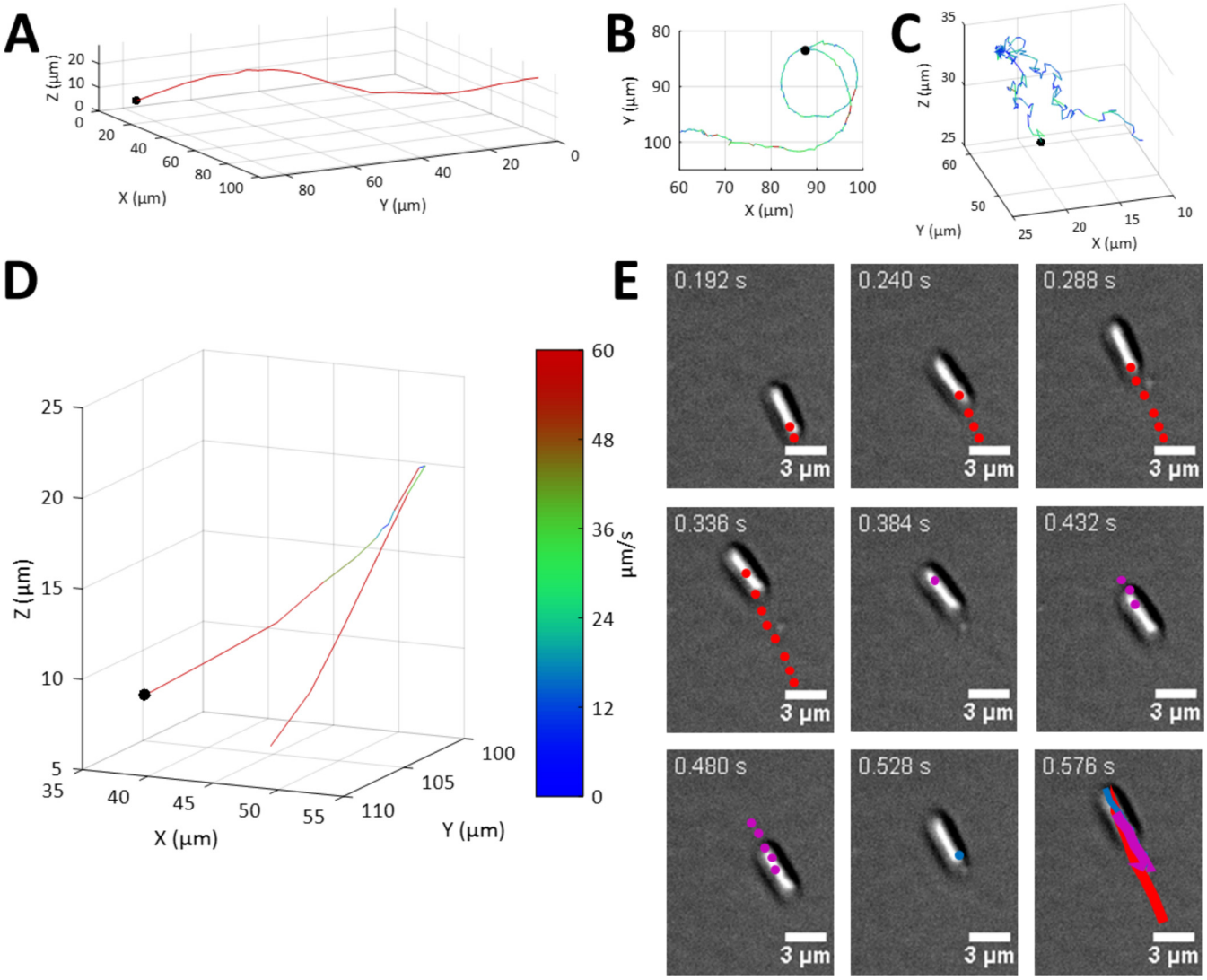

FIG 4 Characterization of bacterial swimming trajectories. (A to C) A number of different trajectory phenotypes were observed, including a run trajectory characterized by relatively long stretches of uninterrupted straight motion (track duration = 1.536 s) (A), near-surface run with increased curvature (track duration = 4.872 s) (B), and oscillating trajectories characterized by frequent changes in direction (track duration = 9.840 s) (C). A black dot marks the beginning of each track. The track is colored by the instantaneous speed according to the intensity scale shown in panel D. (D) Example of bacterial reversal directional change as observed by DHM within the bulk. The start of the trajectory is indicated by a black dot. The track is colored by the instantaneous speed according to the intensity scale. Track duration = 0.720 s. (E) Image sequence of two reversal events measured at the surface by DIC. The time between images is 48 ms. The center of mass of the cell from previous frames is shown as colored dots. The trajectory consists of the sequence forward-reverse-forward, and each segment has been colored red-magenta-blue, respectively. The entire trajectory is shown as colored lines on the final image shown. The two reversal events were observed at around 0.336 s and 0.480 s, whereupon the cell was observed to pause for a frame such that the center of mass of the cell remained unchanged between two frames.

reversal events being caused by a change in flagellum rotational direction inducing a reversal of the bacterial direction of travel without reorientation of the bacterial body (35). To observe this more closely, we imaged cells using a third of the camera's chip size, enabling a higher acquisition rate, 333 Hz. At this higher frame rate we were still unable to observe any reorientation of the bacteria (Movie S3). Moreover, equipping the microscope with a fluorescence filter set enabled the use of total internal reflectance fluorescence (TIRF) imaging in order to visualize flagella through the use of fluorescent staining. Using this approach, flagella were readily observed at both the leading and trailing ends of bacteria before and after surface reversal events (Fig. S2C and Movie S4), showing that *P. aeruginosa* cells are able to use their flagella to both push and pull, consistent with previous observations for monotrichous bacteria (36–38).

We observed no statistical differences in the speed of bacterial trajectories before and after reversal events (Fig. S2D).

Stationary cells at the surface were found attached either horizontally or vertically (long axis or pole attached). Long-axis-attached cells were identified from DIC images in which the distinct rod shape of the bacteria was observed and remained stationary throughout the duration of an image sequence, with no change in the center of mass of the cell (Fig. 2C). In contrast, pole-attached bacteria were observed to be smaller and circular, and small deviations in a cell's center of mass were observed as the cell wobbled on a single attachment point (Fig. 2C). In some cases, pole-attached cells were observed to be spinning due to the flagella being fixed to the surface while the bacteria body remained free and able to rotate, a phenomenon observed previously (8) (Movie S5).

Exploring the respective contributions of the MotAB and MotCD stators to swimming motility. To exemplify the applications of the multimode microscope, we investigated the relative contributions of the MotAB and MotCD stators to swimming motility by comparing the trajectories of the *P. aeruginosa* wild type (WT) and the corresponding *motAB*, *motCD*, and *motABCD* deletion mutants in order to assess cell behavior both within the bulk and at the surface. By tracking bacteria over a 2.4-s interval (Fig. 5), we first characterized the trajectories of each strain to determine whether the different forms of cellular movement apparent on visual inspection of cell tracking videos could be quantitatively categorized. As anticipated, the *motABCD* mutant was nonmotile (15, 19), with all trajectories observed from this strain having a speed below 10 μm/s and a slope of the log plot (K_{MSD}) below 1.5 (Fig. S3P). The average speed and K_{MSD} observed for this strain were 5.3 μm/s and 0.86, respectively. Therefore, the *motABCD* mutant was not analyzed further.

Cell tracks were quantitatively characterized by instantaneous speed, total displacement, and their mean square displacement (MSD) over the time range (δt) of 50 to 1,000 ms (Fig. S3A to I). The K_{MSD} was used to assess the directionality of a track, whereby a slope of <1 suggests constrained motion, a slope of 1 suggests Brownian diffusion, and a slope of >1 suggests active motion (Fig. S3A to I) (39–41).

Considering the mean speed and K_{MSD} together, it was evident that two trajectory types were apparent in the *P. aeruginosa* wild-type population at both the surface and in the bulk (Fig. S3J to O). A cluster of tracks was observed for cells with a mean velocity above 30 μm/s and a K_{MSD} above 1.5, with the remaining trajectories having a mean velocity below 20 μm/s or a K_{MSD} below 1. A similar grouping of trajectories was observed for the *motAB* and *motCD* mutants, although in both cases the separation of the two groups was less evident due to a reduction in the velocity observed for the directionally swimming bacteria (Fig. S3K and L). Trajectories were separated into two classes; the first included bacterial tracks with a high velocity (>25 μm/s) and a high K_{MSD} (>1.5), while the second group was formed by the remainder. Plots of the resulting tracks divided into the two classes are shown in Fig. 5. It was evident that based upon the selection criteria described, the trajectories separated into two clearly distinct motility types; in the first, the bacteria moved over large distances in a highly directional manner which have previously been described as runs (Fig. 4A), and in the second, frequent reversals in direction, termed oscillating, were evident (Fig. 4C). Trajectories that remained at the surface were assigned as rambling as opposed to oscillating. We assigned runs that remained near the surface (within the focal plane of DIC images) for greater than 1 s as near-surface runs (Fig. 4B). We were thus able to automatically assign the trajectory type and exclude the possibility of operator bias. The different bacterial trajectories were individually assessed to determine frequency, average speed, and K_{MSD} (Table 1).

Using the analysis described, trajectory types were compared at the surface and within the bulk. The bulk bacterial wild-type trajectories were predominantly (64%) runs, at an average speed of 59 $\pm$ 4 μm/s (mean $\pm$ standard deviation). In comparison, both *motAB* and *motCD* mutants were predominately oscillating ($\approx$54%) and the average run speed was significantly ($P < 0.0001$) reduced in both cases, to 29 $\pm$ 9 μm/s

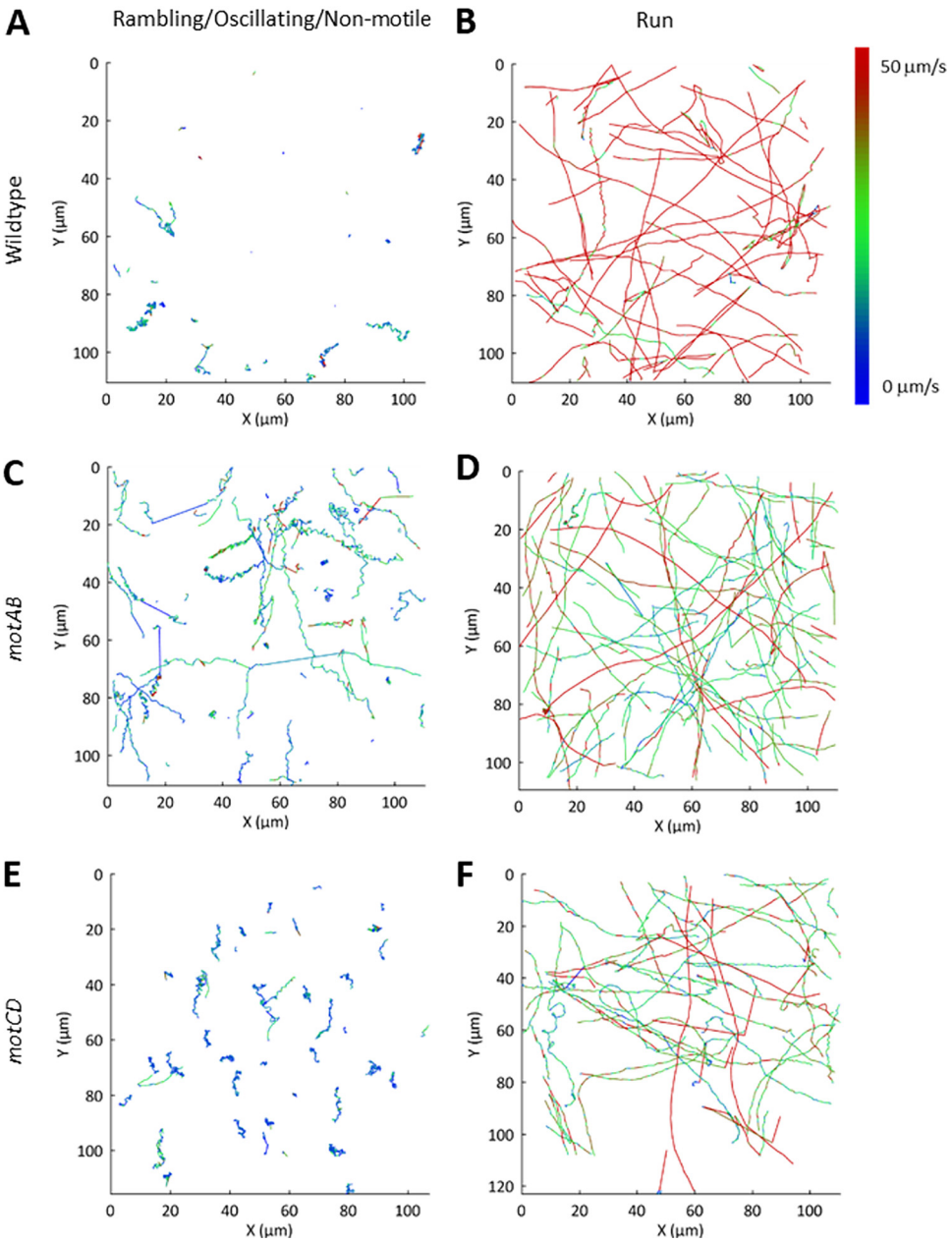

FIG 5 Top view of bacterial trajectories for *P. aeruginosa*. (A and B) Wild type; (C and D) *motAB* mutant; (E and F) *motCD* mutant. Trajectories are colored according to the speed (see intensity scale). Trajectories have been split into rambling/oscillating/nonmotile (A, C, and E) and run (B, D, and F).

and 45 ± 18 μm/s, respectively (Fig. 6A and Table 1). This average measure of single-cell bacterial swimming contrasts with conventional measurements of population swimming speeds in low-viscosity agar, in which under these conditions no change in speed was observed for the *P. aeruginosa motAB* and *motCD* mutants (20). In this prior study, different classes of motility were not taken into account.

Increased variance in the speed within a single run trajectory was observed for the *motCD* mutants in the bulk (average standard deviation = 32 ± 36 μm/s, compared with 18 ± 4 μm/s and 9 ± 1 μm/s for the wild-type and *motAB* strains, respectively [Fig. 6A and Table 1]). Thus, removal of the *motCD* stator reduced the ability of the bacteria to swim at a constant speed.

The average speed of near-surface runs was significantly ($P < 0.01$) reduced compared to the average run speed in the bulk for all strains, by 7%, 39%, and 51% for the

TABLE 1 Summary of quantification of surface tracks, including both surface and bulk measurements[a]

	Surface						Bulk					
	WT		*motAB* mutant		*motCD* mutant		WT		*motAB* mutant		*motCD* mutant	
Parameter	Mean	SD	Mean	SD	Mean	SD	Mean	SD	Mean	SD	Mean	SD
Classification of cells												
No. of tracks	150		138		142		71		154		97	
Motile (%)	27	±6	77	±9	77	±20	97	±7	97	±3	100	±0
Runs (% of motile cells)	51	±6	10	±2	25	±28	64	±31	45	±10	46	±34
Near-surface runs (% of motile cells)	18	±9	54	±4	43	±16						
Rambling (surface)/oscillating (bulk) (% of motile cells)	31	±12	36	±5	32	±21	36	±31	55	±10	54	±34
Attached (%)	72	±9	23	±9	21	±22						
Polar attached (% of attached cells)	30	±14	73	±26	55	±31						
Long-axis attached (% of attached cells)	70	±14	27	±26	45	±31						
Floating (%)	2	±3	0	±1	2	±3	3	±7	3	±3	0	±0
Direction change analysis												
Frequency of reversal events for cell runs (Hz)	0.9	±0.4	0.2	±0.0	0.6	±0.3	0.5	±0.1	0.1	±0.0	0.1	±0.1
Oscillating frequency							3.1	±1.0	1.5	±1.0	2.6	±0.6
Rambling frequency (Hz)	3.2	±2.1	2.9	±1.5	6.1	±0.7						
Arrival and departure from the surface												
Attachment rate (% of nonattached cells/s)	0.2	±0.4	0.3	±0.4	0.8	±0.7						
Detachment rate (% of attached cells/s)	0.2	±0.3	2.2	±2.5	2.5	±1.6						
Motility characterization												
	Surface run						Run					
Speed (μm/s)	55	±7	18	±5	22	±21	59	±4	29	±9	45	±18
Speed variance	23	±6	10	±6	16	±12	18	±4	9	±1	32	±36
K_{MSD} ($\mu m^2/s$)	1.9	±0.2	1.9	±0.3	1.8	±0.2	1.9	±0.3	1.8	±0.4	1.9	±0.2
	Rambling						Oscillating					
Speed (μm/s)	18	±8	13	±4	12	±4	12	±5	19	±5	10	±2
Speed variance	11	±5	8	±4	11	±3	11	±8	9	±2	5	±1.3
K_{MSD} ($\mu m^2/s$)	1.7	±0.3	1.7	±0.4	1.5	±0.4	1.2	±1	1.6	±0.4	1.3	±0.3

[a]Speeds presented are the average speeds measured over frame intervals of 24 ms. Speed variance is the average standard deviation for the instantaneous speeds measured for an entire trajectory. The ranges quoted are 1 standard deviation of such measurements for each cell. WT, wild type.

wild type and *motAB* and *motCD* mutants, respectively (Fig. 6A and B and Table 1). Thus, strains lacking either stator reduced their speed more significantly at the surface than the wild-type strain and, therefore, either reduced their power input or were unable to achieve the same speed for a certain power input within the fluid dynamics experienced at the liquid-solid interface (42, 43). This demonstrates a difference in the responses to the surface between the stator mutants and the WT, consistent with a key role for the stators in responding to the surface environment as bacterial cells shift from the bulk environment to the near-surface environment. In this study, observation of the differential behavior of the bacteria at the surface and bulk was achieved through the interlaced capture of cells both within the bulk and at the surface. The directionality of the run trajectories for all strains (including the wild type) was unaltered either in the bulk or at the surface, with a K_{MSD} of 1.8 to 1.9 observed in all cases (Table 1).

In an oscillating trajectory, the bacteria rapidly changed direction (Fig. 4C) as a result of the reversal of bacterial flagellar rotation (Fig. 4E). Both the wild type and *motCD* mutant had high oscillating frequencies, 3.1 ± 1.0 Hz and 2.6 ± 0.6 Hz, respectively, whereas the *motAB* mutant exhibited a reduced oscillating frequency, 1.5 ± 1.0 Hz (significant at a *P* value of <0.05) (Table 1). The average instantaneous speed of the oscillating *motAB* mutant was also higher (19 ± 5 μm/s) than those of the two other strains (≈11 μm/s [Table 1]). As oscillating trajectories were observed for both mutants, either stator appears to be sufficient to support this type of trajectory. However, the altered phenotype of the *motAB* mutant suggests a possible role for MotAB in controlling the oscillatory trajectory. The directionality of the oscillating trajectories over a δt of 50 to 1,000 ms also varied between the two mutants. The K_{MSD} values of 1.2 to 1.6

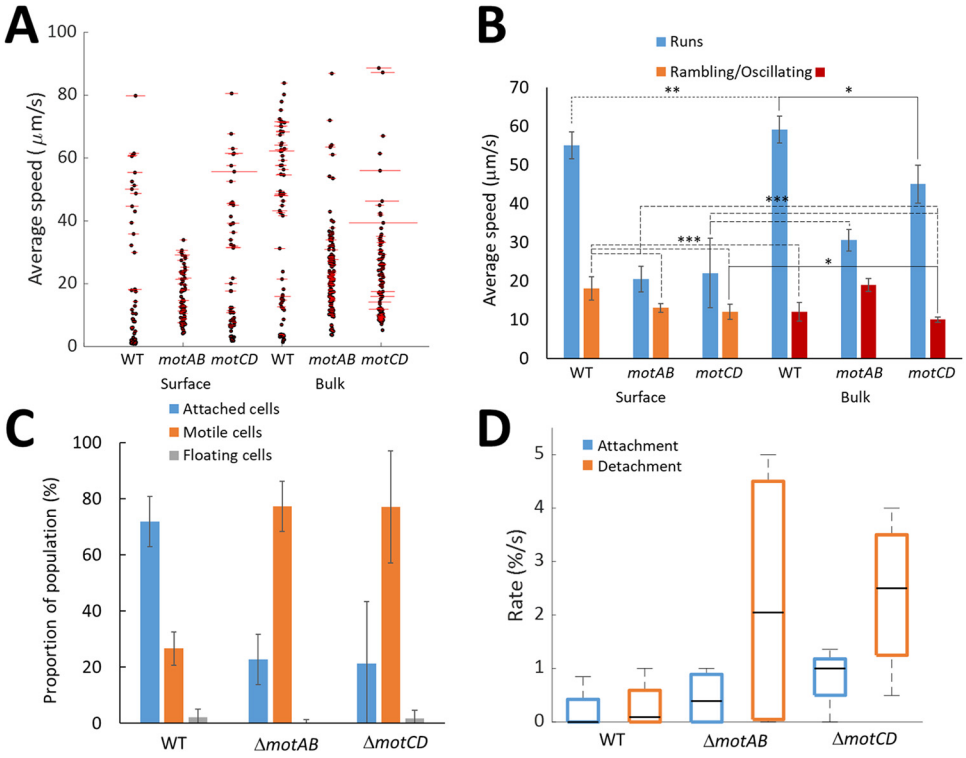

FIG 6 Comparison of the surface (DIC) and bulk (DHM) motilities of the *P. aeruginosa* wild type and *motAB* and *motCD* mutants. (A) Comparison of the bulk and surface runs for speed. Each black dot is the measured average speed for a trajectory, while the length of the associated red line is proportional to the SD of the speed measured between frames over the trajectory length. (B) Comparison of the average speed measured for the run, oscillating, and rambling trajectories of the *P. aeruginosa* wild type and *motAB* and *motCD* mutants. The mean value was taken by averaging the speeds across 5 biological replicates. Error bars equal ±95% confidence limits. Statistically significant differences are shown as follows: * and solid line, $P < 0.05$; ** and dotted line, $P < 0.01$; and *** and dashed line, $P < 0.001$. The lack of a difference and differences with P values of <0.0001 are not shown. (C) Assessment of the attachment profile for each bacterial strain, reporting the total proportion of attached cells, motile cells, and floating cells. Error bars equal ±1 SD unit ($n = 5$). (D) Box-and-whisker plot for the attachment and detachment rates measured at the surface and reported as the percentage of nonattached cells attaching per second or the percentage of attached cells detaching per second. The central black line marks the median and the top and bottom of the box indicate the 75th and 25th percentiles, respectively, while the whiskers extend to the maximum and minimum values ($n = 5$).

were lower than the run trajectories; thus, this trajectory type allowed the bacteria to move in a more diffusive manner. A statistically significant increase in K_{MSD} was observed for the *motAB* mutant compared with both the wild type ($P = 0.04$) and *motCD* mutant ($P = 0.001$) that is consistent with the oscillating trajectory requiring a contribution from MotAB.

A statistically significant ($P < 0.001$) reduction in average speed was observed between the run and rambling trajectories at the surface for the wild-type and *motAB* strains but not for the *motCD* mutant due to the high variability in the speed of surface runs for different trajectories observed for this strain (Table 1). The reduction in average speed from 22 to 12 μm/s for surface runs and rambling, respectively, for the *motCD* mutant was consistent with the other strains. For all strains a statistically significant ($P < 0.05$) reduction in directionality from a K_{MSD} of 1.8 to 1.9 to 1.5 to 1.7 was observed. No significant difference in the K_{MSD} values for the rambling trajectories of the different strains was observed.

In addition, surface attachment, detachment, and reversals for the *mot* mutants were also compared. After 5 min a larger proportion (72%) of the wild-type cells were attached to the surface than for either of the *mot* mutants (≈22%) (Fig. 6C). Among the attached cells, variance was also observed in the ratio of pole-attached to long-axis-attached cells, with values of 0.42, 2.7, and 1.2 observed for the wild type and

motAB and *motCD* mutants, respectively (Table 1). Switching from long-axis to polar attachment has previously been associated with cell surface departure (7). Consistent with this, Fig. 6D shows that although no statistically significant differences were observed between the attachment rates, the detachment rates for both mutants were higher (≈2.3% of attached cells per second) than for the wild type (0.2% of attached cells per second). Path deviations greater than 120 degrees, classified as reversals, were observed very infrequently for runs or rambling tracks. The highest reversal rates were observed for the wild-type bacteria (0.5 ± 0.1 Hz), while the *mot* mutants had similar reversal rates, 0.1 ± 0.1 Hz. The reversal rates for all strains increased when the bacteria were involved in near-surface runs. While for both wild type and the *motAB* mutant, reversal rates increased 2-fold upon exposure to the surface, for the *motCD* mutant, reversals increased 6-fold (Table 1). This result contrasts with reversal rates observed previously for *P. aeruginosa* strain PA14 (15), where the reversal rates observed for the respective *motAB* and *motCD* mutants were 2- to 3-fold higher than for the wild type. This is likely due to the different *P. aeruginosa* strain or the culture conditions used; specifically, the PA14 experiments were conducted using stationary-phase bacteria grown in M63 medium supplemented with glucose and with the addition of 3% Ficoll to increase growth medium viscosity and so slow motility to enable imaging. The load responses of MotAB and MotCD stators have also been well studied (18), and the order-of-magnitude difference we observed in the reversal rates of the *motAB* and *motCD* mutants was likely a response to the variation in viscosity. Together, these results suggest that the stators are involved in determining the outcome of *P. aeruginosa* cell interactions with a surface, consistent with previous observations (15). A few nonmotile cells (<2%) were observed for all motile strain populations. We also observed flagellum-driven spinning for 10 to 13% of attached cells for all bacterial strains with the exception of the *motABCD* mutant, for which no spinning was observed, consistent with the flagellum-dependent nature of this phenotype (8).

As the motility of log-phase bacterial cells was investigated, we observed individual cells in various stages of cell division. To assess the influence of cell division on motility, we compared the trajectories of bacteria undergoing cell division identified via their elongated shapes. The near-surface swimming behavior of dividing cells was unchanged compared with that of nondividing cells, with no statistically significant differences observed between the speed or directionality of runs. However, the average speed of swimming, dividing cells was reduced from 40 ± 28 μm/s to 30 ± 17 μm/s, suggesting that during cell division, bacteria swim more slowly, likely as a result of the energetic costs of dividing, competition between the two daughter cell flagella that may not be fully formed, and the increased drag associated with a larger cell body.

To assess the role of the bacterial stators in bacterial surface accumulation, we observed the distributions of the *P. aeruginosa* wild type and *mot* mutants after 2 h of growth. Histograms of the bacterial distribution in the z-axis are shown in Fig. 7. A higher association of the wild type and the *motAB* mutant with the two glass surfaces compared to the bulk was observed, both at the top and at the bottom (Fig. 7). For the wild-type bacteria the cell fraction (per micrometer) was more than 15 times greater within 5 μm of the top and bottom surfaces than near the surface (5 to 20 μm) or within the middle of the sample chamber (20 to 50 μm). Assessment of the cell track classifications revealed that the surface accumulation was due to both near-surface swimming and surface attachment. The surface accumulation observed for the *motAB* mutant was significant ($P < 0.05$) but not as great as for the wild type, with the cell fraction per micrometer at the top and bottom surfaces exceeding the middle of the sample chamber by 6 to 8 times. The cell fraction per micrometer was twice as great for the top and bottom surfaces for the *motCD* mutant compared with the middle of the chamber, while for the *motABCD* mutant only the bottom surface showed a difference from the other regions. These differences, however, were not statistically significant ($P > 0.05$). The minimal surface accumulation for the nonmotile *motABCD* mutant was as anticipated given its lack of a flagellum. For the *motCD* mutant, the reduction of surface accumulation suggests a role for MotCD in surface sensing during

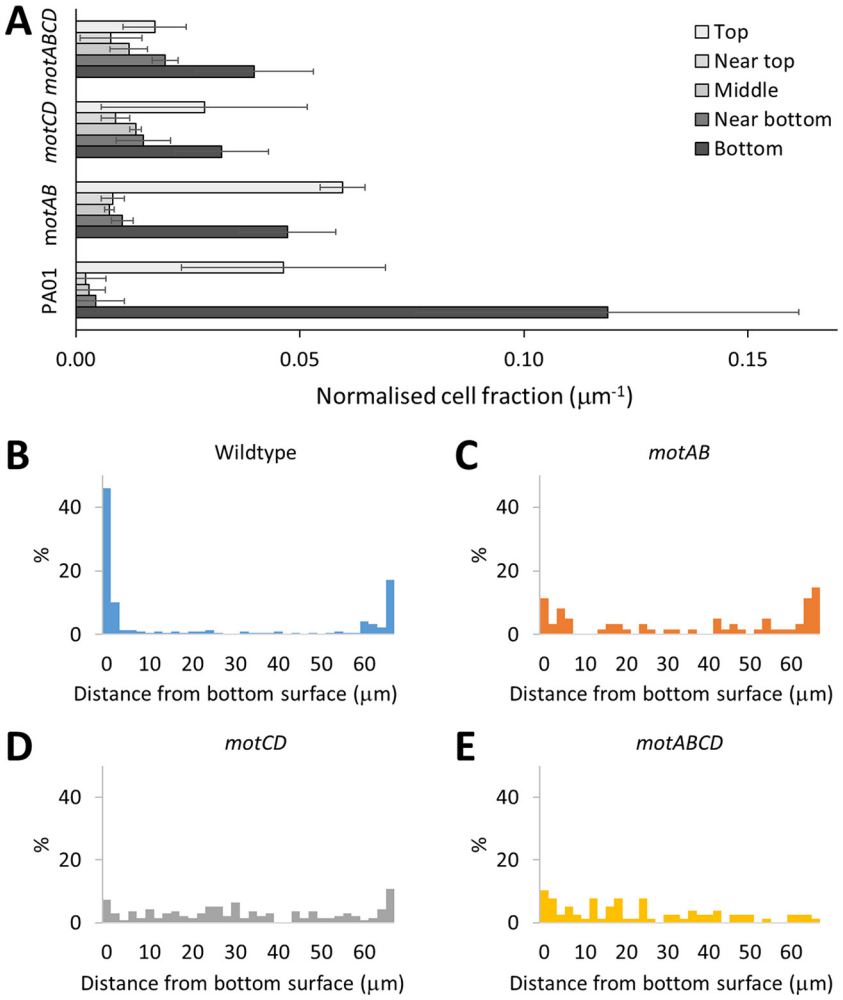

FIG 7 Investigation of surface accumulation of bacteria. (A) The normalized cell fraction (normalized to unit length in z axis) observed at varied z-regions within the sample chamber. Nonnormalized data are shown in panels B to E. Regions studied were bottom and top areas equal to 0 to 5 μm from the surface, near the top and bottom equal to 5 to 20 μm from the surface, and the middle region. The average numbers of bacteria measured within the volume for each strain after the 5 min were as follows: wild type, 54; *motAB* mutant, 21; *motCD* mutant, 27; and *motABCD* mutant, 15. Error bars equal $\pm$1 SD unit from 3 biological replicates. The area imaged was 120 by 120 μm. (B to E) Fractions of bacterial population within different z-segments within a glass sandwich taken approximately 5 min after addition to chamber. Data are presented as a percentage of the total number of cells observed in the z-stack.

the initial attachment stages. Moreover, the similar bulk and surface distributions of the motile *motCD* mutant suggest that the surface accumulation of bacteria cannot be explained by hydrodynamic or steric forces alone but may additionally be actively achieved by altered bacterial behavior when sensing a surface. No statistically significant differences were observed between the top and bottom surfaces for any of the bacterial strains, suggesting that neither gravity, buoyancy, nor chemotaxis/aerotaxis was a controlling factor in this experimental setup ($P > 0.06$).

DISCUSSION

P. aeruginosa adopts one of two major lifestyles, a free-living motile or a surface-associated, sessile lifestyle (8, 12, 14). Understanding how bacteria make decisions to switch between such lifestyles is important for unlocking new strategies for the prevention and treatment of bacterial infections, especially biofilm-centered infections given their chronicity and resistance to host defenses and antibiotics. The key role of surfaces in bacterial lifestyle choices highlights the importance of developing methods that are able to capture quantitatively the differences in bacterial behavior within

populations at the surface and in the bulk in order to provide new insights into bacterial surface sensing. To this end, we have developed a multimode microscope with dual surface/bulk imaging capabilities allowing the observation of subtle differences in the bacterial trajectories of *P. aeruginosa* cells within the bulk and the near-surface environment.

Characterization of bacterial trajectories revealed two types of motility that were consistent with previous studies (27, 35) and could be categorized by consideration of speed and directionality. Notably, although runs were observed both at the surface and in the bulk, oscillatory trajectories were observed only within the bulk, while rambling trajectories were observed only at the surface. Deletion of either stator did not inhibit any trajectory type, demonstrating that a specific stator complex was not associated with a specific trajectory type. However, the oscillatory frequency for the *motAB* mutant was reduced compared to that of the WT, suggesting a role for this stator in regulating this particular trajectory type. It was not clear what caused the bacteria to exhibit a particular trajectory type; however, the lower speed and decreased directionality of the rambling and oscillatory trajectory types suggest an explorative behavior in contrast to runs, which allow bacteria to travel more rapidly over larger distances. Adopting the rambling or oscillatory trajectories also enables bacterial cells to alter direction in a manner similar to the tumbling action observed for the peritrichous *E. coli* (2).

A greater distribution of average speeds was noted for cells within the *motCD* mutant population as a consequence of the greater variability in the speed of an individual cell than for the WT or *motAB* mutant. Previous studies have demonstrated that bacteria are able to control their torque through regulating the turnover of stator units (44, 45). The variability in the speed of the *motCD* mutants compared with the WT and *motAB* mutants suggests a greater variability in the number of stator units within the flagellar complex across the population.

While the WT strain's swimming speed was statistically indistinguishable between bacteria swimming at the surface and those within the bulk, the *motAB* and *motCD* mutants' swimming speed at the surface was significantly ($P < 0.0001$) slower than within the bulk. It is possible that either the WT is able to adjust to the altered physicochemical near-surface environment or to obstruction of flagellar rotation by the surface due to the exchange of the two stator complexes to modulate flagellar torque. Stator exchange has been proposed to act as a signaling mechanism in concert with c-di-GMP within *P. aeruginosa* (6, 11, 17). The absence of either stator within the *motAB* and *motCD* mutants removes the option for stator exchange, preventing the cells from being able to either sense or respond to the near-surface environment using this mechanism.

The involvement of both bacterial appendages, flagella and pili, in bacterial swarming, biofilm formation, and, ultimately, surface sensing has been reported previously (4, 10, 12, 17, 46). In *P. aeruginosa*, flagellar signaling involves c-di-GMP and the diguanylate cyclase SadC (17), while pili, particularly TFP, are able to mechanically interact with a surface through successive pilus extension and retraction that enables signal transduction through the Chp system to regulate cyclic AMP levels (13). While the mechanosensing role of pili for regulating the behavior of surface-associated bacteria is clear, our results and those of others (4) also support a role for the flagellum in surface sensing.

Here we have also shown that both the *motAB* and *motCD* mutant populations included a higher proportion of detached cells and that attached cells were more likely to detach, further demonstrating the differential surface response of *P. aeruginosa* caused by the deletion of either of the flagellar stators. This is likely caused by the inability of the bacteria to sense the surface effectively, so they fail to trigger the upregulation of c-di-GMP and pili required for cells to become irreversibly surface attached, leading to biofilm formation. The similar behaviors of the two *mot* mutants suggest that both stators are involved in the cell signaling, potentially through stator exchange. The absence of surface accumulation noted only for the *motCD* mutant,

however, indicates a greater role for the MotCD stator in surface sensing and subsequent biofilm formation.

In summary, we have developed a multimode 2/3D microscope that combines DIC, DHM, TIRM, and TIRF imaging modes to achieve simultaneous bulk and surface label-free imaging of single cells in a motile bacterial population. The microscope was used to investigate the role of the *P. aeruginosa motAB* and *motCD* flagellar stators on motility and surface interactions, enabling observations of altered phenotypic behavior of cells located within the bulk or at the surface.

MATERIALS AND METHODS

Bacterial strains and growth conditions. *P. aeruginosa* strain PAO1 (Washington subline) and the isogenic *motAB*, *motCD*, and *motABCD* mutants were each grown at 37°C overnight in lysogeny broth (LB) and diluted to an optical density at 600 nm (OD_{600}) of 0.01 in LB prior to incubation for a further 4 h at 37°C with shaking to reach log phase at an OD_{600} of ≈1. Bacterial cultures were diluted to an OD_{600} of 0.015 in LB before inoculation into analysis chambers. The *mot* mutants were constructed by two-step allelic exchange as previously described (47). Two PCR products amplifying the upstream and the downstream nucleotide regions of *motAB* and *motCD* were generated using the primer pairs 1FW/1RW and 2FW/2RW, respectively (Table S1). Both PCR products were fused by overlapping PCR to create a deletion in the corresponding gene. The resulting fragment was cloned into the suicide plasmid pME3087 (48). Following transformation into the target strain by conjugation, single crossovers were selected on tetracycline (125 μg·ml^{-1}). The double-crossover mutants were selected by carbenicillin enrichment (47). After 3 rounds of counterselection, the resulting *P. aeruginosa* colonies were screened for the loss of antibiotic resistance by plating on LB supplemented or not with tetracycline. The in-frame deletions were confirmed by PCR and DNA sequence analysis.

For genetic complementation of the in-frame deletion mutants, the *motAB* and *motCD* genomic regions were PCR amplified using *P. aeruginosa* chromosomal DNA as a template and the primer pairs indicated in Table S1. The purified fragments were cloned into the shuttle vector pME6032 (49). The insertions were verified by restriction enzyme and sequence analysis and introduced into the *motAB* and *motCD* mutants by electroporation. The swarming ability of the *mot* mutants was verified by swarming plate assays (data not shown).

Sample chamber. Two strips of double-sided tape, approximately 2 by 15 by 0.1 mm, were placed on a borosilicate glass coverslip (VWR) in parallel with a gap of ~4 mm. A second glass coverslip was placed on top of the double-sided tape to create a chamber with a floor and ceiling of glass and walls of double-sided tape. The second coverslip was rotated 45° to allow ease of loading the channel with growth medium (Fig. 1C). After inoculation with bacteria, the two ends of the chamber were sealed using silicone-free grease (Apiezon).

Microscopy. Imaging was achieved using a bespoke multimode microscope (Fig. 1A) (Cairn Ltd.). Samples were analyzed at 37°C using a Nikon Eclipse Ti inverted microscope using a 60× oil objective (NA = 1.49; working distance [WD] = 0.13 mm). The microscope was fitted with an environmental chamber (Okolab) to regulate temperature, relative humidity, and CO_2. Images were acquired using an Orca-Flash 4.0 digital complementary metal oxide semiconductor (CMOS) camera (Hamamatsu) at a typical acquisition rate of 41.6 Hz. DIC imaging was achieved using a single-channel white MonoLED (Cairns) light source. A polarizer was inserted above the condenser, and Wollaston prisms were inserted between the condenser and polarizer and below the objective. Use of the prisms did not adversely affect DHM image quality. In-line DHM imaging was acquired using a 685-nm LX laser (Obis). TIRM was conducted using an Obis 488-nm LX laser (Cairn) controlled using an illumination system (iLas2). The sample was illuminated through the objective by use of a 50% mirror, controlled to achieve total internal reflectance by irradiating the sample at an incidence angle (θ) greater than the critical angle (θ_c) given by equation 1, where n_1 is the refractive index of the incident medium and n_2 is the refractive index of the transmission medium.

$$\sin(\theta_c) = \frac{n_2}{n_1} \tag{1}$$

Bacterial imaging was achieved through the local change in refractive index and θ_c induced upon cells entering the evanescent field caused by the TIR. The penetration depth (d) of the evanescent field was determined using equation 2, where θ is the wavelength of the light (488 nm) and tuned to 200 nm.

$$d = \frac{\lambda}{4\pi}\left[n_1^2 sin^2(\theta) - n_2^2\right]^{-1/2} \tag{2}$$

A total of 5 biological repeats for each mutant was prepared and imaged by interlaced capture of DHM with either DIC or TIRM. Each image sequence consisted of 2,000 frames (1,000 frames for each acquisition mode) for a total duration of 48 s.

The optical requirements of DHM, DIC, and TIRM were met without interfering with the other imaging modes; thus, multimode acquisition could be achieved by modulating the intensity of the different illumination sources. Different modes of acquisition could not be acquired simultaneously but required interlaced capture achieved through computer control. The limiting factor in the time resolution of bacterial motion capture was the frame rate of the camera, which in this case was 100 Hz.

z-stack images were acquired using a bespoke remote focusing assembly as described previously (30).

To sample the early stages of bacterial cell surface attachment, *P. aeruginosa* was inoculated into the sample chamber at an OD_{600} of 0.015 in LB. Bacteria were observed to undergo cell division within the chamber for 4 to 6 h until reaching stationary phase.

To observe flagellar orientation during reversals, PAO1 was fluorescently stained using Alexa Fluor carboxylic acid succinimidyl esters (Alexa Fluor 488; Thermo Fisher). PAO1 cells were grown overnight in LB medium at 37°C and 200 rpm, resuspended, and diluted in fresh LB medium at an OD_{600} of 0.01. When cells reached exponential phase, they were centrifuged at 2,000 × *g* for 10 min and the growth medium was removed. The cell pellet was gently resuspended in a wash buffer of 10^{-2} M KPO_4, 6.7×10^{-2} M NaCl, and 10^{-4} M EDTA, with pH adjusted to 7.0 with HCl, and centrifuged. After two additional rinses, cells were incubated with 0.5 mg/ml of Alexa Fluor 488 carboxylic acid succinimidyl ester for 1 h at room temperature with gentle rocking. Residual dye was removed after washing twice, and the cells were resuspended in phosphate-buffered saline (PBS) for imaging.

Image processing. After acquisition, holograms were processed using a bespoke Matlab script (Text S1, ImageProcess). Image intensity across a stack was normalized; the median image over the stack was subtracted to remove background signal, including attached cells. DHM image output sequences were reconstructed using a bespoke Python package (See-Through Scientific) (28; contact irwin@see-through.com for further information), making use of Rayleigh-Sommerfeld formalism to determine bacterial x-y-z coordinates. Bacterial trajectories were determined using a bespoke Matlab script (Text S1, DHMTracking). To exclude noise, a voxel limit was set and applied to each image such that similar numbers of objects were identified in each frame. Visual inspection of interferogram image sequences enabled an estimate of the number of bacteria per frame to ensure that the voxel limit was set so as not to exclude bacterial cells. Bacterial trajectories were determined using the bespoke Matlab script (Text S1, Tracking). Objects were matched with their nearest neighbor within the next frame, applying a distance limit based upon the maximum speed of bacteria (100 μm/s). The script looked up to 4 frames ahead for a matching object. All tracks were also visually inspected using a bespoke Matlab script (Text S1, Graphing) to ensure that trajectories skipping more than 4 frames could be joined. All Matlab scripts used for processing the data are presented as part of the supplemental material (Text S1), and the combined DHMTrack project can be accessed at GitHub (https://github.com/fishhooky/DHMTrack).

The mean squared displacement (MSD) of tracks was calculated using a bespoke Matlab script (ROC_MSD) and calculated according to equation 3, where $\vec{x}(t_j) = \vec{R}_j$ and was the vector of the *j*th point on the trajectory and the angled brackets indicate all measurements within a given time t_i (50).

$$\Delta x^2(t) = \left\langle \left[\vec{x}\left(t_{i+1}\right) - \vec{x}\left(t_i\right)\right] \right\rangle^2 \tag{3}$$

DIC images and z-stacks were processed using a bespoke Matlab script (StackMaster). Each image was flattened by a line-by-line polynomial fit. A threshold was then applied to binarize the image to segment pixels with bacteria. The threshold was set as signal²/noise² >10. The square of the signal was measured so as to identify both bright and dark regions associated with the DIC image. Objects less than 20 pixels were excluded as noise. Holes within objects were filled using the Matlab function "imfill." Bright and dark regions were paired based upon proximity and a common directional vector between objects within the same frame. The center of mass of objects was calculated, giving equal weighting to bright and dark regions. The length and width of the smallest rectangle around an object and the orientation of the bacterial cells were determined using a bespoke Matlab script (ParticleAnalysisDIC). For DIC z-stacks, objects on consecutive frames were analyzed to identify overlapping pixels considering the x-y dimensions. If common pixels were identified, objects were grouped to form a single object and the center of mass was determined for this object based upon the combined pixels using a bespoke Matlab script (DICZStack_ImageProcessing). Bacterial trajectories were determined as described for DHM data.

TIRM images were processed using ImageJ 1.50b. When processing interlaced DHM and TIRM images, the center of mass of moving cells as determined by DHM was shifted to the average position between two adjacent frames to account for the 20-ms offset between the capture of TIRM and DHM images.

Statistical analysis. Differences between data sets were assessed using unpaired *t* tests or one-way analysis of variance (ANOVA) as appropriate to determine the *P* value. The value *n* indicates the number of biological replicates. Error bars indicate ±1 standard deviation unit.

SUPPLEMENTAL MATERIAL

Supplemental material for this article may be found at https://doi.org/10.1128/mSystems.00390-19.

MOVIE S1, AVI file, 2.2 MB.
MOVIE S2, AVI file, 0.9 MB.
MOVIE S3, AVI file, 1.8 MB.
MOVIE S4, AVI file, 0.03 MB.
MOVIE S5, AVI file, 1.6 MB.
TEXT S1, TXT file, 0.1 MB.
FIG S1, TIF file, 0.1 MB.
FIG S2, TIF file, 1.3 MB.
FIG S3, TIF file, 0.3 MB.
TABLE S1, PDF file, 0.4 MB.

ACKNOWLEDGMENTS

This work was supported via Wellcome Trust joint senior investigator awards (grant nos. 103882 and 103884). A. L. Hook also thanks the University of Nottingham for funding via his awarded Nottingham Research Fellowship.

We declare no competing conflicts of interest.

Kind assistance from Andrew Woodward with Matlab scripts is acknowledged.

REFERENCES

1. Xie L, Altindal T, Chattopadhyay S, Wu XL. 2011. Bacterial flagellum as a propeller and as a rudder for efficient chemotaxis. Proc Natl Acad Sci U S A 108:2246–2251. https://doi.org/10.1073/pnas.1011953108.
2. Berg HC, Brown DA. 1972. Chemotaxis in Escherichia coli analysed by 3-dimensional tracking. Nature 239:500–504. https://doi.org/10.1038/239500a0.
3. Wood TK, Barrios AFG, Herzberg M, Lee J. 2006. Motility influences biofilm architecture in Escherichia coli. Appl Microbiol Biotechnol 72:361–367. https://doi.org/10.1007/s00253-005-0263-8.
4. Laventie BJ, Sangermani M, Estermann F, Manfredi P, Planes R, Hug I, Jaeger T, Meunier E, Broz P, Jenal U. 2019. A surface-induced asymmetric program promotes tissue colonization by Pseudomonas aeruginosa. Cell Host Microbe 25:140–152.e6. https://doi.org/10.1016/j.chom.2018.11.008.
5. O'Toole GA, Wong GC. 2016. Sensational biofilms: surface sensing in bacteria. Curr Opin Microbiol 30:139–146. https://doi.org/10.1016/j.mib.2016.02.004.
6. Baker AE, Diepold A, Kuchma SL, Scott JE, Ha DG, Orazi G, Armitage JP, O'Toole GA. 2016. PilZ domain protein FlgZ mediates cyclic di-GMP-dependent swarming motility control in Pseudomonas aeruginosa. J Bacteriol 198:1837–1846. https://doi.org/10.1128/JB.00196-16.
7. Conrad JC. 2012. Physics of bacterial near-surface motility using flagella and type IV pili: implications for biofilm formation. Res Microbiol 163:619–629. https://doi.org/10.1016/j.resmic.2012.10.016.
8. Conrad JC, Gibiansky ML, Jin F, Gordon VD, Motto DA, Mathewson MA, Stopka WG, Zelasko DC, Shrout JD, Wong GCL. 2011. Flagella and pili-mediated near-surface single-cell motility mechanisms in P. aeruginosa. Biophys J 100:1608–1616. https://doi.org/10.1016/j.bpj.2011.02.020.
9. Ellison CK, Rusch DB, Brun YV. 2019. Flagellar mutants have reduced pilus synthesis in Caulobacter crescentus. J Bacteriol 201:e00031-19. https://doi.org/10.1128/JB.00031-19.
10. Kohler T, Curty LK, Barja F, van Delden C, Pechere JC. 2000. Swarming of Pseudomonas aeruginosa is dependent on cell-to-cell signaling and requires flagella and pili. J Bacteriol 182:5990–5996. https://doi.org/10.1128/JB.182.21.5990-5996.2000.
11. Kuchma SL, Delalez NJ, Filkins LM, Snavely EA, Armitage JP, O'Toole GA. 2015. Cyclic di-GMP-mediated repression of swarming motility by Pseudomonas aeruginosa PA14 requires the MotAB stator. J Bacteriol 197:420–430. https://doi.org/10.1128/JB.02130-14.
12. O'Toole GA, Kolter R. 1998. Flagellar and twitching motility are necessary for Pseudomonas aeruginosa biofilm development. Mol Microbiol 30:295–304. https://doi.org/10.1046/j.1365-2958.1998.01062.x.
13. Persat A, Inclan YF, Engel JN, Stone HA, Gitai Z. 2015. Type IV pili mechanochemically regulate virulence factors in Pseudomonas aeruginosa. Proc Natl Acad Sci U S A 112:7563–7568. https://doi.org/10.1073/pnas.1502025112.
14. Sauer K, Camper AK, Ehrlich GD, Costerton JW, Davies DG. 2002. Pseudomonas aeruginosa displays multiple phenotypes during development as a biofilm. J Bacteriol 184:1140–1154. https://doi.org/10.1128/jb.184.4.1140-1154.2002.
15. Toutain CM, Caizza NC, Zegans ME, O'Toole GA. 2007. Roles for flagellar stators in biofilm formation by Pseudomonas aeruginosa. Res Microbiol 158:471–477. https://doi.org/10.1016/j.resmic.2007.04.001.
16. Kearns DB. 2010. A field guide to bacterial swarming motility. Nat Rev Microbiol 8:634–644. https://doi.org/10.1038/nrmicro2405.
17. Baker AE, Webster SS, Diepold A, Kuchma SL, Bordeleau E, Armitage JP, O'Toole GA. 2019. Flagellar stators stimulate c-di-GMP production by Pseudomonas aeruginosa. J Bacteriol 201:e00741-18. https://doi.org/10.1128/JB.00741-18.
18. Baker AE, O'Toole GA. 2017. Bacteria, rev your engines: stator dynamics regulate flagellar motility. J Bacteriol 199:e00088-17. https://doi.org/10.1128/JB.00088-17.
19. Doyle TB, Hawkins AC, McCarter LL. 2004. The complex flagellar torque generator of Pseudomonas aeruginosa. J Bacteriol 186:6341–6350. https://doi.org/10.1128/JB.186.19.6341-6350.2004.
20. Toutain CM, Zegans ME, O'Toole GA. 2005. Evidence for two flagellar stators and their role in the motility of Pseudomonas aeruginosa. J Bacteriol 187:771–777. https://doi.org/10.1128/JB.187.2.771-777.2005.
21. Valentini M, Filloux A. 2016. Biofilms and cyclic di-GMP (c-di-GMP) signaling: lessons from Pseudomonas aeruginosa and other bacteria. J Biol Chem 291:12547–12555. https://doi.org/10.1074/jbc.R115.711507.
22. Hug I, Deshpande S, Sprecher KS, Pfohl T, Jenal U. 2017. Second messenger-mediated tactile response by a bacterial rotary motor. Science 358:531–534. https://doi.org/10.1126/science.aan5353.
23. Frymier PD, Ford RM, Berg HC, Cummings PT. 1995. Three-dimensional tracking of motile bacteria near a solid planar surface. Proc Natl Acad Sci U S A 92:6195–6199. https://doi.org/10.1073/pnas.92.13.6195.
24. Taute KM, Gude S, Tans SJ, Shimizu TS. 2015. High-throughput 3D tracking of bacteria on a standard phase contrast microscope. Nat Commun 6:8776. https://doi.org/10.1038/ncomms9776.
25. Li GL, Bensson J, Nisimova L, Munger D, Mahautmr P, Tang JX, Maxey MR, Brun YV. 2011. Accumulation of swimming bacteria near a solid surface. Phys Rev E 84:041932. https://doi.org/10.1103/PhysRevE.84.041932.
26. Wu MM, Roberts JW, Buckley M. 2005. Three-dimensional fluorescent particle tracking at micron-scale using a single camera. Exp Fluids 38:461–465. https://doi.org/10.1007/s00348-004-0925-9.
27. Vater SM, Weiße S, Maleschlijski S, Lotz C, Koschitzki F, Schwartz T, Obst U, Rosenhahn A. 2014. Swimming behavior of Pseudomonas aeruginosa studied by holographic 3D tracking. PLoS One 9:e87765. https://doi.org/10.1371/journal.pone.0087765.
28. Flewellen JL, Zaid IM, Berry RM. 2019. A multi-mode digital holographic microscope. Rev Sci Instrum 90:023705. https://doi.org/10.1063/1.5066556.
29. Bianchi S, Saglimbeni F, Leonardo RD. 2017. Holographic imaging reveals the mechanism of wall entrapment in swimming bacteria. Phys Rev X 7:011010. https://doi.org/10.1103/PhysRevX.7.011010.
30. Botcherby EJ, Juskaitis R, Booth MJ, Wilson T. 2008. An optical technique for remote focusing in microscopy. Opt Commun 281:880–887. https://doi.org/10.1016/j.optcom.2007.10.007.
31. Berg HC, Turner L. 1995. Cells of Escherichia coli swim either end forward. Proc Natl Acad Sci U S A 92:477–479. https://doi.org/10.1073/pnas.92.2.477.
32. Berke AP, Turner L, Berg HC, Lauga E. 2008. Hydrodynamic attraction of swimming microorganisms by surfaces. Phys Rev Lett 101:038102. https://doi.org/10.1103/PhysRevLett.101.038102.
33. Shum H, Gaffney EA, Smith DJ. 2010. Modelling bacterial behaviour close to a no-slip plane boundary: the influence of bacterial geometry. Proc R Soc A Math Phys Eng Sci 466:1725–1748. https://doi.org/10.1098/rspa.2009.0520.
34. Bartholomew JW. 1949. Flagellation of certain species of Pseudomonas as seen with the electron microscope. J Gen Microbiol 3:340–346. https://doi.org/10.1099/00221287-3-3-340.
35. Taylor BL, Koshland DE, Jr. 1974. Reversal of flagellar rotation in monotrichous and peritrichous bacteria: generation of changes in direction. J Bacteriol 119:640–642.
36. Hintsche M, Waljor V, Grossmann R, Kuehn MJ, Thormann KM, Peruani F, Beta C. 2017. A polar bundle of flagella can drive bacterial swimming by pushing, pulling, or coiling around the cell body. Sci Rep 7:16771. https://doi.org/10.1038/s41598-017-16428-9.
37. Ping LY. 2012. Cell orientation of swimming bacteria: from theoretical simulation to experimental evaluation. Sci China Life Sci 55:202–209. https://doi.org/10.1007/s11427-012-4298-7.
38. Cai QX, Li ZJ, Ouyang Q, Luo CX, Gordon VD. 2016. Singly flagellated

Pseudomonas aeruginosa chemotaxes efficiently by unbiased motor regulation. mBio 7:e00013-16. https://doi.org/10.1128/mBio.00013-16.
39. Theves M, Taktikos J, Zaburdaev V, Stark H, Beta C. 2013. A bacterial swimmer with two alternating speeds of propagation. Biophys J 105:1915–1924. https://doi.org/10.1016/j.bpj.2013.08.047.
40. Wu XL, Libchaber A. 2000. Particle diffusion in a quasi-two-dimensional bacterial bath. Phys Rev Lett 84:3017–3020. https://doi.org/10.1103/PhysRevLett.84.3017.
41. Bouchaud JP, Georges A. 1990. Anomalous diffution on disordered media—statistical mechanisms, models and physical applications. Phys Rep 195:127–293. https://doi.org/10.1016/0370-1573(90)90099-N.
42. van Loosdrecht MC, Lyklema J, Norde W, Zehnder AJ. 1990. Influence of interfaces on microbial activity. Microbiol Rev 54:75–87.
43. Zhu YX, Granick S. 2001. Viscosity of interfacial water. Phys Rev Lett 87:096104. https://doi.org/10.1103/PhysRevLett.87.096104.
44. Leake MC, Chandler JH, Wadhams GH, Bai F, Berry RM, Armitage JP. 2006. Stoichiometry and turnover in single, functioning membrane protein complexes. Nature 443:355–358. https://doi.org/10.1038/nature05135.
45. Blair DF, Berg HC. 1988. Restoration of torque in defective flagellar motors. Science 242:1678–1681. https://doi.org/10.1126/science.2849208.
46. Rashid MH, Kornberg A. 2000. Inorganic polyphosphate is needed for swimming, swarming, and twitching motilities of Pseudomonas aeruginosa. Proc Natl Acad Sci U S A 97:4885–4890. https://doi.org/10.1073/pnas.060030097.
47. Malone JG, Jaeger T, Manfredi P, Dotsch A, Blanka A, Bos R, Cornelis GR, Haussler S, Jenal U. 2012. The YfiBNR signal transduction mechanism reveals novel targets for the evolution of persistent Pseudomonas aeruginosa in cystic fibrosis airways. PLoS Pathog 8:e1002760. https://doi.org/10.1371/journal.ppat.1002760.
48. Voisard C, Bull CT, Keel C, Laville J, Maurhofer M, Schnider U, Defago G, Haas D. 1994. Biocontrol of root diseases by Pseudomonas fluorescens CHA0: current concepts and experimental approaches, p 67–89. *In* O'Gara F, Dowling DN, Boesten B (ed), Molecular ecology of rhizosphere microorganisms: biotechnology and the release of GMOs. VCH Verlagsgesellschaft mbH, Weinheim, Germany.
49. Heeb S, Itoh Y, Nishijyo T, Schnider U, Keel C, Wade J, Walsh U, O'Gara F, Haas D. 2000. Small, stable shuttle vectors based on the minimal pVS1 replicon for use in gram-negative, plant-associated bacteria. Mol Plant Microbe Interact 13:232–237. https://doi.org/10.1094/MPMI.2000.13.2.232.
50. Utada AS, Bennett RR, Fong JCN, Gibiansky ML, Yildiz FH, Golestanian R, Wong GCL. 2014. Vibrio cholerae use pili and flagella synergistically to effect motility switching and conditional surface attachment. Nat Commun 5:4913. https://doi.org/10.1038/ncomms5913.